

RESEARCH ARTICLE

10.1002/2016GC006753

Key Points:

- We demonstrate for the first time that magnetic nanoparticle inclusions within silicates can be paleomagnetically important
- Remanence acquisition in biogenic magnetite is more efficient than in detrital titanomagnetite inclusions within silicates
- Assessment of paleomagnetic recording of each magnetic component needs to become a routine part of sedimentary RPI analysis

Correspondence to:

A. P. Roberts,
andrew.roberts@anu.edu.au

Citation:

Chen, L., D. Heslop, A. P. Roberts, L. Chang, X. Zhao, H. V. McGregor, G. Marino, L. Rodriguez-Sanz, E. J. Rohling, and H. Pälike (2017), Remanence acquisition efficiency in biogenic and detrital magnetite and recording of geomagnetic paleointensity, *Geochem. Geophys. Geosyst.*, 18, doi:10.1002/2016GC006753.

Received 29 NOV 2016

Accepted 14 MAR 2017

Accepted article online 17 MAR 2017

Remanence acquisition efficiency in biogenic and detrital magnetite and recording of geomagnetic paleointensity

Liang Chen^{1,2}, David Heslop¹ , Andrew P. Roberts¹ , Liao Chang^{1,3} , Xiang Zhao¹ , Helen V. McGregor^{1,4}, Gianluca Marino¹ , Laura Rodriguez-Sanz¹ , Eelco J. Rohling^{1,5} , and Heiko Pälike⁶

¹Research School of Earth Sciences, Australian National University, Canberra, Australian Capital Territory, Australia, ²South China Sea Marine Survey and Technology Center, State Oceanic Administration, Guangzhou, China, ³Now at School of Earth and Space Sciences, Peking University, Beijing, China, ⁴Now at School of Earth and Environmental Sciences, University of Wollongong, Wollongong, New South Wales, Australia, ⁵Ocean and Earth Science, National Oceanography Centre, University of Southampton, Southampton, UK, ⁶Center for Marine Environmental Sciences, University of Bremen, Bremen, Germany

Abstract Relative paleointensity (RPI) variations of Earth's magnetic field are widely used to understand geomagnetic field behavior and to develop age models for sedimentary sequences. RPI estimation is based on a series of assumptions. One key assumption that is rarely considered is that all magnetic particles in the sediment acquired a magnetization in an identical manner. In this paper, we test this assumption for sediments from the eastern equatorial Pacific Ocean that record well-documented global RPI variations over the last ~780 kyr. The magnetization is carried by two stable single domain magnetic components, which we identify as magnetite magnetofossils and titanomagnetite nanoparticle inclusions within larger silicate particles. By analyzing signals carried by the two components separately, we determine for the first time that magnetic nanoparticle inclusions can cause their host particles to record reliable but inefficient sedimentary paleomagnetic signals. The magnetization carried by biogenic magnetite is acquired more efficiently than that carried by the nanoparticle inclusions. Variations in the concentration of both components are modulated climatically so that they record nearly identical RPI signals. In many sediment types, there is no correlation between the concentrations of different magnetic components so that variable remanence acquisition efficiency will complicate RPI recording. Our work demonstrates that detailed assessment of paleomagnetic recording by each constituent magnetic component needs to become a routine part of sedimentary RPI analysis.

1. Introduction

Relative paleointensity (RPI) variations of Earth's magnetic field have been used widely to date sediments [Guyodo and Valet, 1999; Laj et al., 2000; Stoner et al., 2002; Valet et al., 2005; Yamazaki and Oda, 2005; Chanell et al., 2009, 2016; Ziegler et al., 2011]. Compared to geomagnetic polarity reversals, which typically occur at a frequency of several per million years, RPI variations can provide continuous geomagnetic field records at up to millennial to multimillennial resolution. Like geomagnetic reversals, RPI variations are suitable for global correlation because the signal is dominated by the dipole field. Such a globally coherent geophysical signal is useful for dating marine sediments because it is independent of seawater chemistry and, therefore, provides independent dating compared to paleoceanographic proxies (e.g., foraminiferal $\delta^{18}\text{O}$ variations). For example, $\delta^{18}\text{O}$ changes are not synchronous in the global ocean [Skinner and Shackleton, 2005; Lisiecki and Raymo, 2009], which can affect the accuracy of millennial-scale $\delta^{18}\text{O}$ -based chronologies. Thus, alternative methods, such as RPI analysis, are needed for constructing sedimentary age models (and need to be tested rigorously).

A key assumption in RPI estimation is that the magnetization of a sediment is related linearly to the geomagnetic field strength at the time the sediment acquired its magnetization. Unlike thermoremanent magnetization acquisition in igneous rocks, there is no simple constant of proportionality to calibrate the relationship between the natural remanent magnetization (NRM) of a sediment sample and the strength of

the magnetizing field [Tauxe, 1993; Roberts *et al.*, 2013a]. This is because the NRM can be influenced by many factors, including the ambient geomagnetic field strength, the grain size and concentration of the magnetic mineral that records the paleomagnetic signal, and the mechanism(s) by which the magnetic mineral records the geomagnetic field. An empirical approach is generally used to reduce the effects of variations in magnetic mineral grain size and concentration, whereby an artificial laboratory-induced magnetization is imparted to samples and is used to normalize the NRM [Levi and Banerjee, 1976]. A linear relationship between NRM and magnetizing field has been documented for magnetite within a narrow grain size and concentration range. Strict criteria have, therefore, been developed so that RPI analyses should only be conducted on sediments in which magnetite is the NRM-carrying mineral and where the magnetite has limited variations in grain size and concentration [King *et al.*, 1983; Tauxe, 1993]. These criteria ensure that the sediment is effectively magnetically homogeneous, so that non-geomagnetic factors are limited when extracting RPI signals. Several independent lines of evidence indicate that these empirical criteria can be applied successfully to enable extraction of records of relative geomagnetic intensity variations from sediments [Tauxe, 1993; Valet *et al.*, 2005; Roberts *et al.*, 2013a].

Field intensity variations for the last few million years are summarized in composite RPI stacks [Valet *et al.*, 2005; Channell *et al.*, 2009, 2016; Ziegler *et al.*, 2011]. While RPI analysis has successfully documented geomagnetic variations, we lack a detailed understanding of RPI signal recording [Roberts *et al.*, 2013a]. We present new RPI data from the eastern equatorial Pacific Ocean for the last ~780 ka to address this question. As shown below, the paleomagnetic signal is carried by both biogenic and detrital magnetic particles, but few studies provide constraints on the RPI recording capability of these materials. For example, Paterson *et al.* [2013] demonstrated from sediment redeposition experiments that, as is the case for detrital magnetite [Tauxe, 1993], a linear relationship exists between the magnetizing field and the sedimentary magnetization recorded by biogenic magnetite. However, Ouyang *et al.* [2014] demonstrated that these two types of magnetite have markedly different remanence acquisition efficiency (i.e., the fraction of each particle type aligned by the magnetizing field is different). This is an important consideration for RPI analysis. In this study, we assess the relative efficiency of remanence acquisition in biogenic and detrital magnetite for well-dated sediments that record a clear RPI signal. Our analysis contributes to improving understanding of sedimentary paleomagnetic signal recording.

2. Oceanographic and Geological Setting and Sampling

We studied two sediment cores: a jumbo piston core (RR0603-03JC) and a trigger core (RR0603-03TC) from the same site in the eastern central equatorial Pacific Ocean (02.55°N, 117.92°W) at a water depth of 4195 m (Figure 1). The cores were recovered during the AMAT03 site survey cruise on R/V *Roger Revelle*, which aimed to locate suitable drill sites for Integrated Ocean Drilling Program Expeditions 320 and 321 [Lyle *et al.*, 2006]. Piston coring often fails to recover the surfacemost sediment, so the short trigger core was also taken to recover these sediments. Records from the two cores were spliced together by correlation of sediment physical properties; both $\delta^{18}\text{O}$ and X-ray fluorescence (XRF) data support the splice (Figure 2). It is estimated that the upper ~80 cm of sediment was lost during coring. The piston core is 10.87 m in length and the trigger core is 2.78 m in length. The sediments are dominated by calcareous and siliceous nannofossil ooze and range in color from white to dark grayish brown.

The eastern equatorial Pacific Ocean is one of three major high-nutrient, low-chlorophyll oceanic regions [Edwards *et al.*, 2004; Winckler *et al.*, 2016] and is an important source of carbon to the atmosphere [Takahashi *et al.*, 2009; Martínez-Botí *et al.*, 2015]. Approximately 20–50% of new biological production in the global oceans occurs here [Barber and Chavez, 1991; Loubere, 2000]. The present-day carbonate compensation depth (CCD) lies at about 4800 m in the Pacific Ocean, which is well below the water depth of the core site; carbonate is, therefore, abundant in the cored sediment (Figure 2). The core site lies on the equatorial Pacific sediment bulge, which is a 600 m thick deposit of pelagic carbonate and siliceous ooze and chalk that is elongated roughly parallel to the equator [Mitchell *et al.*, 2003]. Continuous pelagic sedimentation on long timescales in this high-productivity zone means that it has long been the focus of paleoenvironmental and paleomagnetic studies [e.g., Channell and Lanci, 2014].

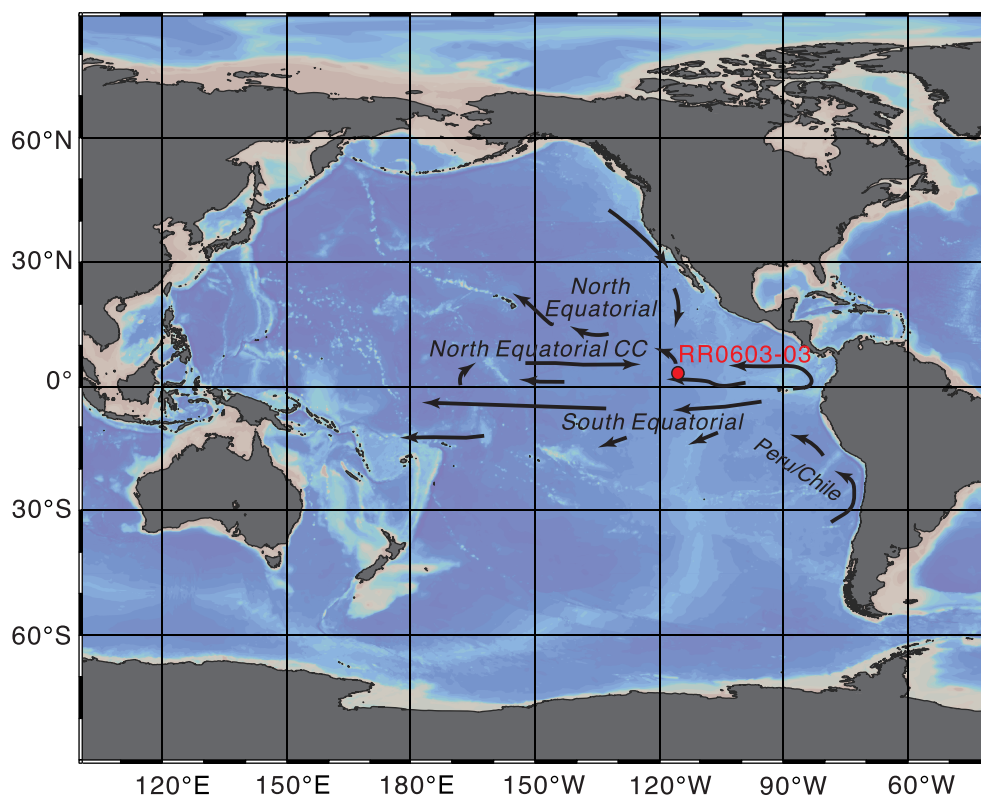


Figure 1. Map of the Pacific Ocean with location of the studied jumbo piston core RR0603-03. Ocean Currents are modified from Wyrski [1966]. CC = Counter Current.

3. Methods

U-channel samples (2×2 cm square cross section and length up to 1.5 m [Weeks *et al.*, 1993]) were collected from the RR0603-03 piston and trigger cores at the Marine Geology Repository, Oregon State University. Paleomagnetic and mineral magnetic measurements were made at the Black Mountain Paleomagnetic Laboratory, Australian National University (ANU). Magnetic measurements were made with a 2-G Enterprises superconducting rock magnetometer at 1 cm intervals. The NRM was subjected to progressive stepwise alternating field (AF) demagnetization at peak fields of 5, 10, 15, 20, 25, 30, 40, 50, 60, 80, 100, 125, and 150 mT. An anhysteretic remanent magnetization (ARM) was imparted in a 0.05 mT direct current (DC) bias field with a superimposed 100 mT peak AF. The ARM was demagnetized at the same field steps used for NRM demagnetization. An isothermal remanent magnetization (IRM) was imparted in a 1-T DC field using a 2-G Enterprises 760 pulse magnetizer, which is treated here as a saturation IRM (SIRM). The IRM was then demagnetized using stepwise peak AFs of 1, 2, 5, 7.5, 10, 12.5, 15, 17.5, 20, 22.5, 25, 27.5, 30, 35, 40, 45, 50, 55, 60, 70, 80, 90, 100, 125, 150, and 170 mT. A 300 mT backfield was applied to all samples after imposing a new SIRM. The remanent magnetization was measured after each field treatment above. In contrast to the high-resolution magnetometers that are typically used for u-channel measurements (spatial resolution of 4–5 cm [Weeks *et al.*, 1993]), the ANU magnetometer has a spatial resolution of ~ 8 cm. While this is not ideal for high-resolution RPI or environmental magnetic analyses, it is adequate for the present study where we aim to assess the relative efficiency of remanence acquisition associated with biogenic and detrital magnetite in sediments rather than to obtain an exceptionally well-resolved RPI record.

Paleomagnetic declination (Dec.) and inclination (Inc.) of the characteristic remanent magnetization (ChRM) were calculated at 1 cm stratigraphic intervals using principal component analysis (PCA) [Kirschvink, 1980]. The closely spaced measurements are not independent because results are smoothed over the 8 cm magnetometer response function window. We present results at 1 cm measurement spacings because neither smoothing nor spatial independence of data are critical for the present study. The uppermost and lowermost 10 cm of data from each u-channel were not used further to avoid issues related to u-channel edge

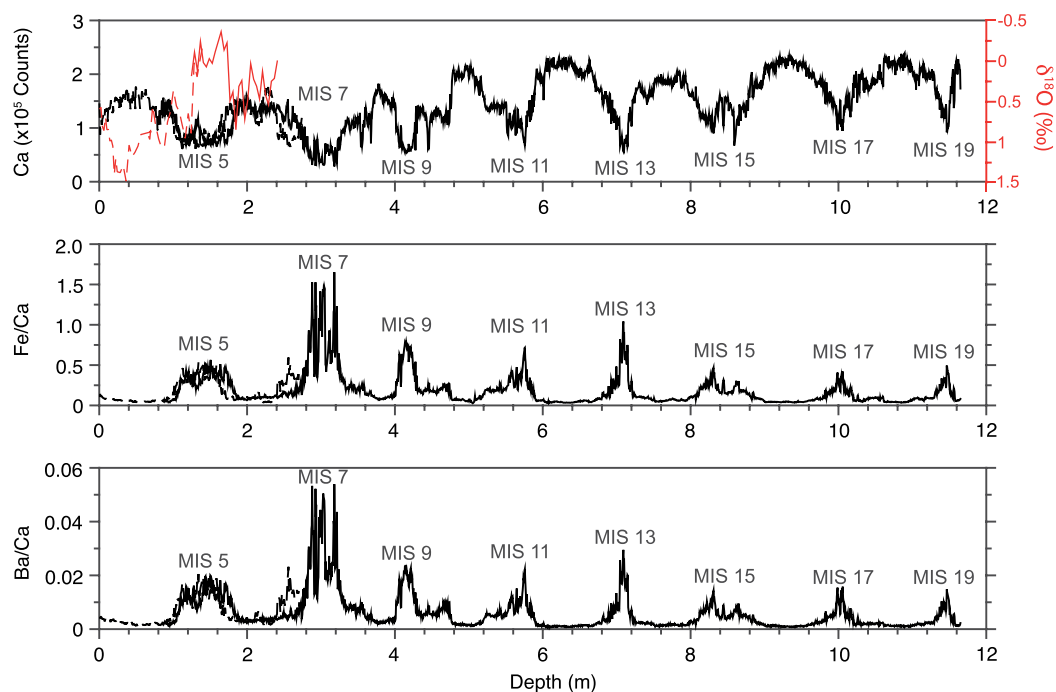


Figure 2. Down-core records of Ca, Fe/Ca, Ba/Ca from core-scanning X-ray fluorescence and $\delta^{18}\text{O}$ from *Neogloboquadrina dutertrei* for core RR0603-03. Marine isotope stage (MIS) positions are indicated. Overlap of data for the trigger core (TC; dashed line) and jumbo piston core (JC; solid line) indicates that the JC did not recover the uppermost part of the record. Ca results indicate biogenic carbonate concentration variations that reflect glacial-interglacial carbonate productivity cycles [e.g., Rea *et al.*, 1991] and provide first-order age constraints for the core. Fe/Ca is a proxy for terrigenous input (mainly eolian dust) to the site [Govin *et al.*, 2012] and Ba is a paleoproductivity proxy in the open ocean [Dymond *et al.*, 1992].

effects. Slopes of NRM/ARM and NRM/IRM over two ranges of demagnetization steps were used to assess how detrital and biogenic magnetic components record RPI signals. Similar approaches have been used for specific demagnetization ranges in different applications [e.g., Channell *et al.*, 2002; Ouyang *et al.*, 2014].

Details of the magnetic mineral assemblage in the studied sediments were explored with mineral magnetic measurements. Hysteresis loops, backfield demagnetization curves, and first-order reversal curves (FORCs) [Pike *et al.*, 1999; Roberts *et al.*, 2000] were measured for samples taken at ~ 20 cm stratigraphic intervals from throughout the jumbo piston core using a Princeton Measurements Corporation MicroMag vibrating sample magnetometer (VSM). Values of the saturation magnetization (M_s), saturation remanent magnetization (M_{rs}), and coercivity (B_c) were obtained from the hysteresis loops, while the coercivity of remanence (B_{cr}) was determined from backfield demagnetization curves. FORC measurements were made using the irregular-grid measurement protocol of Zhao *et al.* [2015]; 140 FORCs were measured with an averaging time of 400 ms. Significance levels (at the 0.05 level) were determined for FORC diagrams following the procedure of Heslop and Roberts [2012a]. Low-temperature magnetic measurements were made with a Quantum Design Magnetic Property Measurement System (MPMS; model XL7), where a SIRM was warmed after samples were cooled to 10 K in either zero field (zero-field cooled; ZFC) or in a 5 T field (field-cooled; FC) [e.g., Moskowitz *et al.*, 1993]. The 5 T field was applied at 10 K and was switched off to impart a low-temperature SIRM; the MPMS magnet was then reset. ZFC and FC curves were measured during zero-field warming in sweep mode at 5 K/min.

Magnetic particles were extracted from bulk sediment with a Frantz isodynamic magnetic separator following Chang *et al.* [2012]. Transmission electron microscope (TEM) observations were made with a JEOL 2100F field emission (FE) TEM operated at 200 kV and a Philips CM300 TEM at 300 kV in the Centre for Advanced Microscopy at ANU. The JEOL 2100F is equipped with a FE gun, an energy-dispersive spectrometer with a silicon drift detector, and scanning TEM (STEM) detectors. STEM observations were performed in the high-angle annular darkfield (HAADF) mode with the JEOL 2100F TEM. The CM300 TEM is equipped with an EDAX Phoenix retractable X-ray detector (ultra-thin window) and a Gatan 694 slow-scan digital camera.

Elemental abundances with glacial-interglacial cyclicity were used to develop an age model for core RR0603-03 that suggested its suitability for the present study [Hale, 2008]. We, therefore, used an ITRAX™ XRF core scanner at the British Ocean Sediment Core Research Facility (BOSCORF) at the National Oceanography Centre, Southampton, to develop a more continuous proxy record for age model construction. In addition, *Neogloboquadrina dutertrei* specimens (80–120 individuals) were picked from the 300–355 μm fraction to develop a planktic foraminiferal $\delta^{18}\text{O}$ record through the last glacial cycle to test the age model based on elemental abundances. To remove potential contaminants and to better homogenize the samples, foraminifera were crushed and cleaned by ultrasonically cleaning them briefly in methanol. An aliquot was taken from each cleaned sample and was analyzed ($\delta^{18}\text{O}$ and $\delta^{13}\text{C}$) at ANU. All measurements were made with a Thermo Finnigan Delta Advantage mass spectrometer coupled to a Kiel IV carbonate device, where samples were reacted with 105% phosphoric acid at 75°C. Results were normalized to the Vienna Peedee Belemnite (VPDB) with the NBS-19 ($\delta^{18}\text{O} = -2.20\text{‰}$, $\delta^{13}\text{C} = 1.95\text{‰}$) and NBS-18 ($\delta^{18}\text{O} = -23.20\text{‰}$, $\delta^{13}\text{C} = 5.014\text{‰}$) carbonate standards. External reproducibility (1σ) for NBS-19 was better than $\pm 0.08\%$ and $\pm 0.06\%$ for $\delta^{18}\text{O}$ and $\delta^{13}\text{C}$, respectively.

4. Results

Down-core XRF elemental abundance variations (Fe/Ca, Ba/Ca) are shown in Figure 2 along with planktic foraminiferal $\delta^{18}\text{O}$ for the last glacial cycle. The most negative $\delta^{18}\text{O}$ values correspond to interglacial MIS 5, where Ca concentrations are low and Fe/Ca and Ba/Ca are high, while the most positive $\delta^{18}\text{O}$ values correspond to the last glacial maximum (MIS 2), where Ca concentrations are high and Fe/Ca and Ba/Ca are low (Figure 2). Anticorrelation between planktic foraminiferal $\delta^{18}\text{O}$ and Ca and positive correlation between $\delta^{18}\text{O}$ and Fe/Ca and Ba/Ca is used to identify glacial-interglacial cyclicity back to marine isotope stage (MIS) 19 (Figure 2). This cyclicity was used to develop an approximate age model for core RR0603-03 (average sedimentation rate of ~ 1.5 cm/kyr). With these data, the boundaries of each MIS are not clearly delineated, so we present results below for core RR0603-03 with respect to depth and compare the positions of MIS boundaries from the SINT-2000 stack [Valet *et al.*, 2005] with those indicated in Figure 2. We compare our record with that of Valet *et al.* [2005] because it has similar temporal resolution to that of our highly smoothed record.

The sediments are stably magnetized, with the NRM decaying univectorially toward the origin of vector component diagrams during progressive AF demagnetization (Figure 3a). ChRM inclinations are shallow and mainly positive (Figure 3b), which is consistent with an expected normal polarity geocentric axial dipole (GAD) field inclination (5.9°) at the site latitude. ChRM declinations are stable for both the trigger and jumbo cores, although they were not oriented azimuthally during coring so the declination was rotated to yield a 0° average for the Brunhes Chron below 1.50 m, which coincides with the expected GAD field declination. Maximum angular deviation (MAD) values from PCA fits are generally $1\text{--}2^\circ$ and most are $<3^\circ$, which demonstrates the high quality of the AF demagnetization data. Inclination and declination data indicate a paleomagnetic reversal at the bottom of the jumbo piston core, which is interpreted to mark the Matuyama-Brunhes (M-B) boundary (~ 780 ka). High MAD values are observed through the M-B boundary (Figure 3b). Care is required in identifying the position of the M-B boundary at the base of the core because the polarity switch could represent a short-period geomagnetic excursion [e.g., Roberts, 2008; Laj and Channell, 2015] rather than a full polarity reversal. Identification of the M-B boundary at the base of the core is consistent with the observed glacial-interglacial elemental abundance cyclicity (Figure 2) where the polarity reversal occurs as expected within MIS 19 [Tauxe *et al.*, 1996; Horng *et al.*, 2002; Liu *et al.*, 2008; Channell *et al.*, 2010; Saganuma *et al.*, 2015]. Thus, although we cannot define precisely the positions of MIS boundaries from Figure 2, these age constraints enable definition of an age model for core RR0603-03 that allows us to test whether a globally coherent RPI signal has been recorded.

When the NRM record for core RR0603-03 is normalized with ARM and IRM, a consistent pattern of RPI variations is evident (Figure 4). The coherency of this signal with the SINT-2000 RPI stack of Valet *et al.* [2005] is evident when plotted with respect to depth (Figure 4) with MIS labels in the same positions as in Figure 2. Age model uncertainties for core RR0603-03 do not affect the RPI record significantly because it is highly smoothed due to the low sedimentation rate and 8 cm measurement smoothing. Overall, core RR0603-03 provides a reasonable estimation of global geomagnetic variations and is suitable for exploring issues

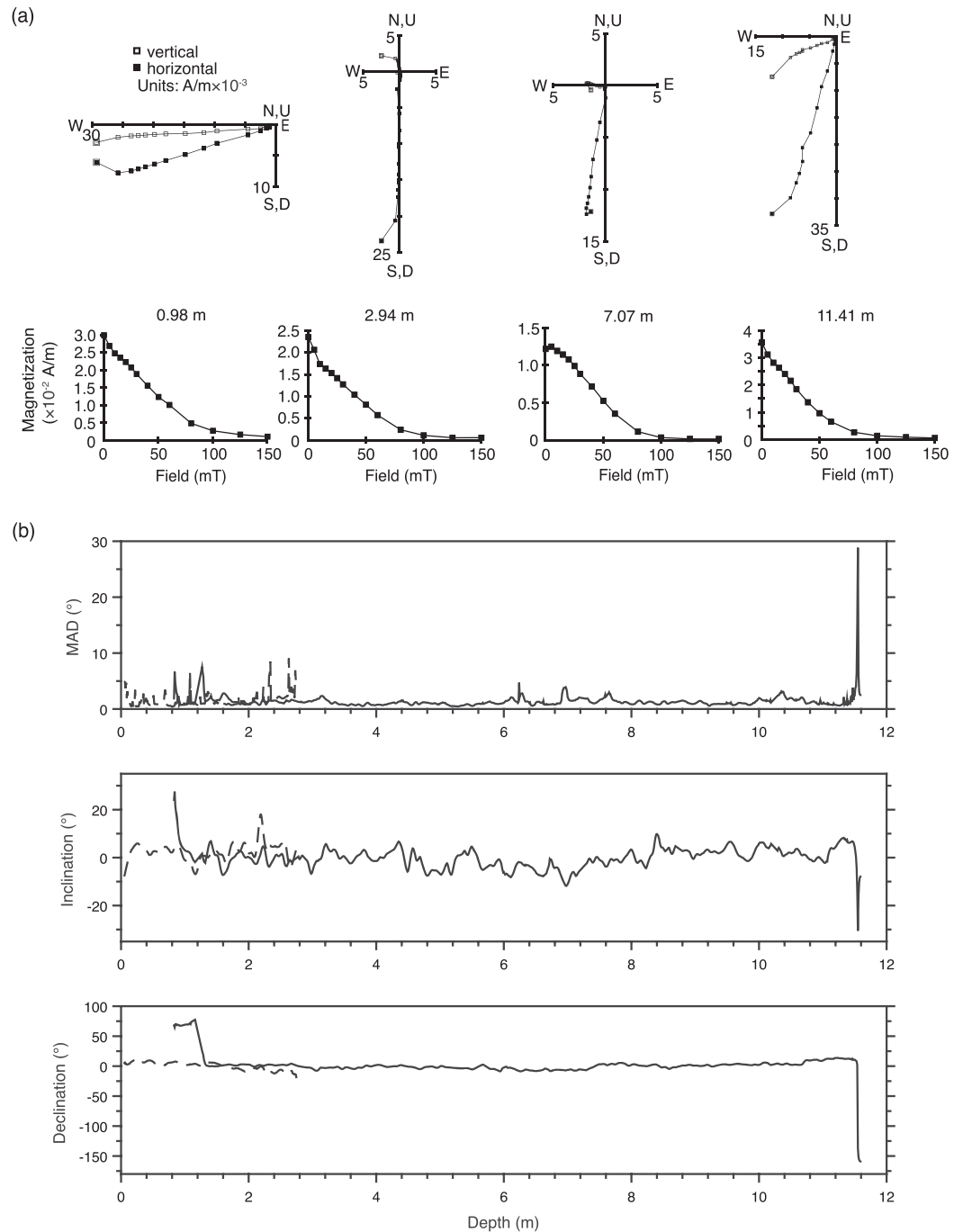


Figure 3. (a) Vector demagnetization diagrams that illustrate the stable paleomagnetic behavior of core RR0603-03 (generated with Puffin-Plot [Lurcock and Wilson, 2012]). (b) Down-core declination (Dec.) and inclination (Inc.) profiles of the characteristic remanent magnetization (ChRM) and maximum angular deviation (MAD) values. The major declination and inclination change at the base of the core represents the Matuyama/Brunhes boundary (consistent with the number of glacial-interglacial cycles (Figure 2) and RPI data (Figure 4)). Data for the trigger core and jumbo core (JC) are indicated with dashed and solid lines, respectively. Anomalous paleomagnetic directions in the upper JC are likely due to sediment disturbance.

concerning RPI recording. Detailed mineral magnetic measurements were, therefore, undertaken to identify the magnetic mineralogy and to assess paleomagnetic recording efficiency.

Hysteresis loops for 70 analyzed samples have similar shapes that reach saturation at or below 200 mT. Values of B_{cr}/B_c versus M_{rs}/M_s cluster within the upper left-hand portion of the pseudo-single-domain (PSD) field of a Day Plot [Day et al., 1977; Dunlop, 2002] (Figure 5a). Sediments generally contain mixtures of

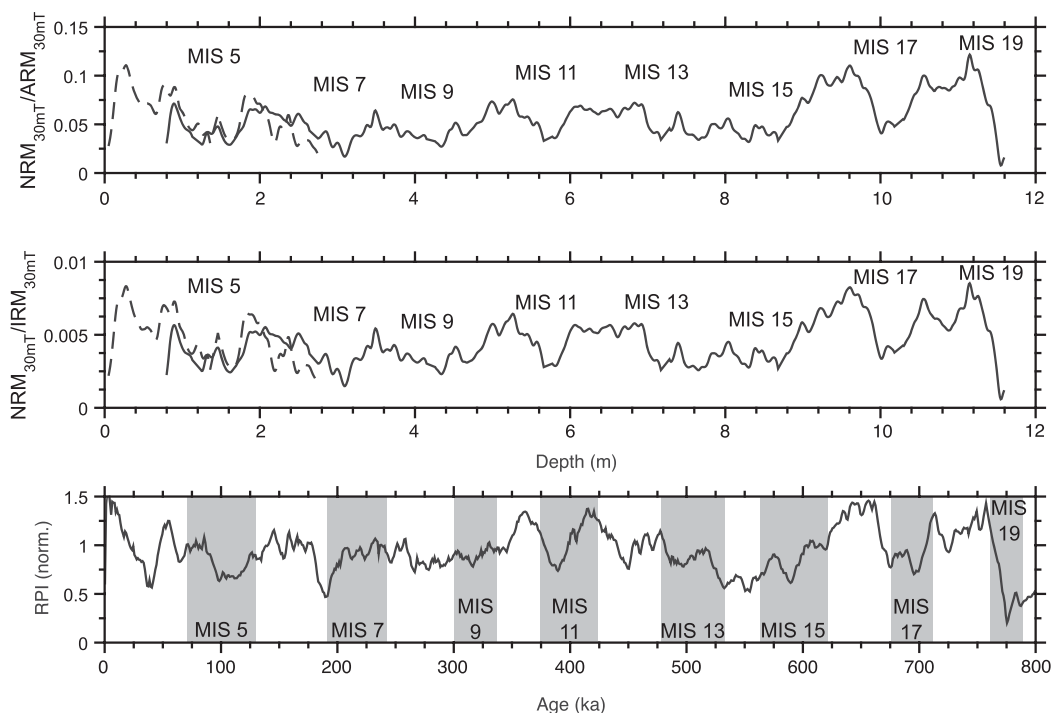


Figure 4. Relative paleointensity (RPI) variations for core RR0603-03 (bulk $\text{NRM}_{30\text{ mT}}/\text{ARM}_{30\text{ mT}}$ and $\text{NRM}_{30\text{ mT}}/\text{IRM}_{30\text{ mT}}$ normalizations) compared to the SINT-2000 record of Valet *et al.* [2005] (bottom). MIS positions are indicated for core RR0603-03 from Figure 2 and for the SINT-2000 RPI stack (odd-numbered MISs are shaded).

multiple magnetic mineral components [e.g., Heslop and Roberts, 2012b; Roberts *et al.*, 2013b; Heslop *et al.*, 2014a], so data for most sediments lie in the middle of the PSD field [Roberts *et al.*, 2012]. A data distribution close to the stable SD field suggests that the magnetization is dominated by SD particles. FORC diagrams (Figures 5b, 5d, 5f, and 5h) have a dominant central ridge signal due to magnetically noninteracting SD particles [Roberts *et al.*, 2000; Egli *et al.*, 2010], which supports this conclusion. Unlike most marine sediments [cf. Roberts *et al.*, 2012], there is only a small signal due to interacting SD or coarser PSD particles that give rise to an asymmetrical, vertically spread FORC distribution that diverges toward the B_i axis [Roberts *et al.*, 2000; Muxworthy and Dunlop, 2002]. Corresponding low-temperature ZFC/FC measurements (Figures 5c, 5e, 5g, and 5i) do not provide evidence for a Verwey transition [Verwey, 1939] at ~ 120 K that would be expected, with slightly different transition temperatures for biogenic and detrital magnetite, if both types of magnetite are present [Chang *et al.*, 2016a]. Low-temperature magnetic results are discussed further below.

IRMs were subjected to a 26-step AF demagnetization sequence. The IRM demagnetization data are smooth and are well fitted with two skewed generalized Gaussian components (Figure 6a) [Egli, 2003; Heslop and Dillon, 2007] that account for 98% of variance in the data set. The contribution of the two components to the IRM varies down-core (Figures 6b and 6c), although the overall shape of the IRM spectra does not vary much (Figure 6d). Average coercivity spectra for the two components for the entire data set are shown in Figure 6a, where the low-coercivity component has a broad and skewed spectrum and the high-coercivity component has a narrow almost log-Gaussian distribution. The low-coercivity component dominates the lower part of the core with contributions of $\sim 60\%$ of the IRM, while above ~ 4 m depth in the core the two components have approximately equal contributions (Figure 6c). The greater contribution of the high-coercivity component above ~ 4 m is also evident in Figure 6d. The low dispersion of the high-coercivity component is consistent with the presence of biogenic magnetite, while the broad distribution of the low-coercivity component is more consistent with a detrital component rather than a second biogenic component [Egli, 2004]. Unusually, the data indicate the presence of two stable SD components, which are interpreted to be due to biogenic and detrital magnetic particles.

Magnetic particles in the studied sediments were explored via TEM imaging of magnetic mineral extracts. Abundant magnetite particles with regular morphology, some of which remain within chain structures,

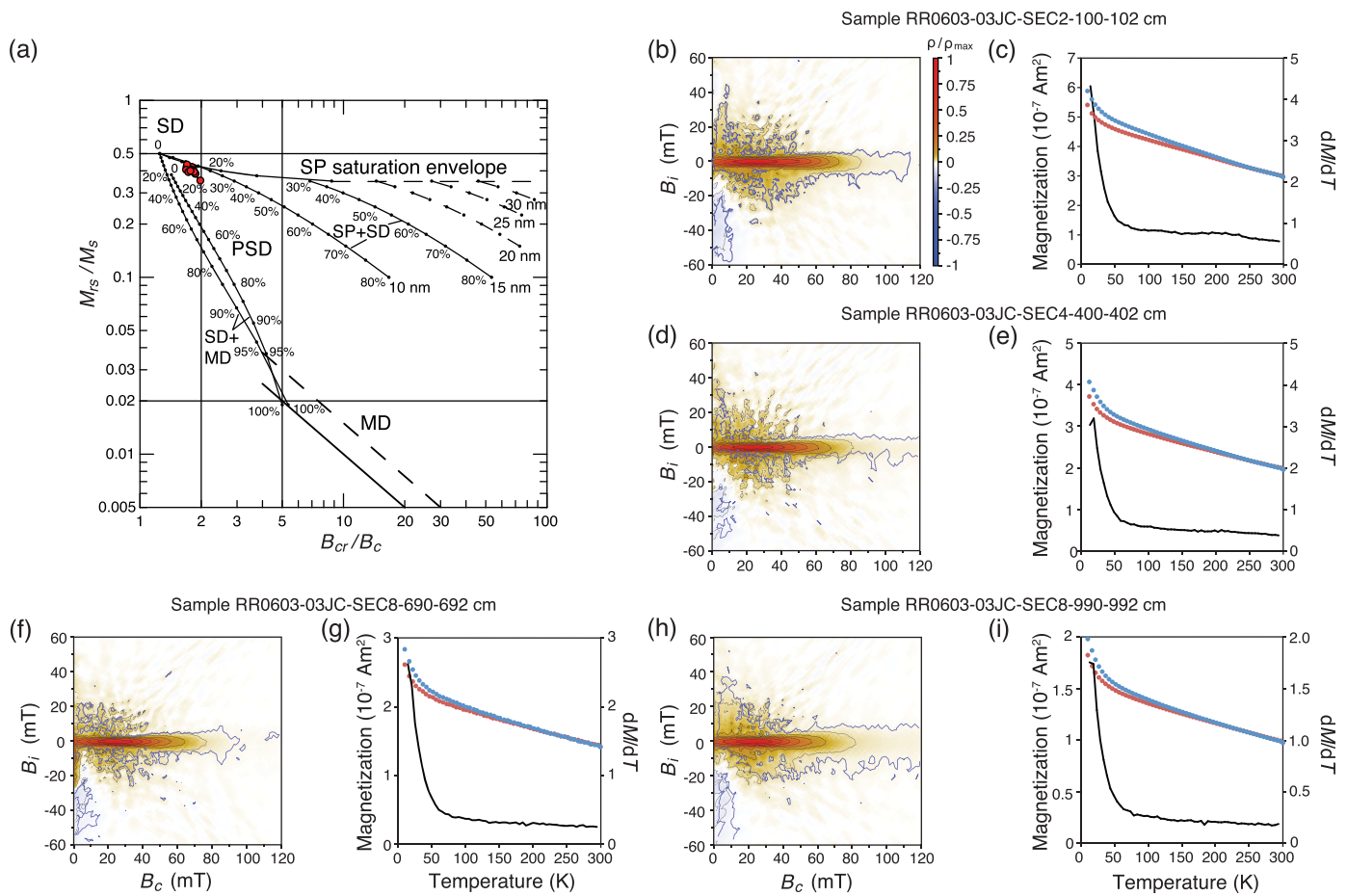


Figure 5. Mineral magnetic results for core RR0603-03. (a) Day plot [Day et al., 1977] (SD = single domain, PSD = pseudosingle domain, and MD = multidomain) with mixing lines for SD+MD and superparamagnetic (SP)+SD mixtures from Dunlop [2002]. Particle sizes in nm and percentages indicate SP particle sizes and concentrations, respectively. While these diagrams are not diagnostically useful for mixed magnetic mineral assemblages [Heslop and Roberts, 2012b], high M_r/M_s values of ~ 0.4 and low B_{cr}/B_c values of < 2.0 indicate magnetic particles close to SD sizes. (b, d, f, h) FORC diagrams for samples from four depths in core RR0603-03, which are indicative of dominantly magnetically noninteracting SD particles with small contributions from interacting SD to PSD particles [cf. Roberts et al., 2000; Muxworthy and Dunlop, 2002; Egli et al., 2010]. Blue contours represent the 0.05 significance level [Heslop and Roberts, 2012a]. (c, e, g, i) Low-temperature ZFC (red) and FC (blue) magnetization curves (left-hand axis) for the same samples. No Verwey transition is indicated in the ZFC curve derivative at ~ 120 K (black, right-hand axis).

represent the inorganic fossilized remains of magnetotactic bacteria (Figures 7a–7d), and provide the strong evidence required to identify magnetofossils [Kopp and Kirschvink, 2008]. These observations confirm indications of the presence of magnetofossils from hysteresis data (Figure 5a), central ridge signatures in FORC diagrams (Figures 5b, 5d, 5f, and 5h), and the high-coercivity component with narrow dispersion from IRM decomposition analysis (Figure 6a). Such combined observations have been made frequently from sediments in recent years [Egli et al., 2010; Roberts et al., 2011, 2012, 2013b; Yamazaki, 2012; Yamazaki and Ikehara, 2012; Larrasoana et al., 2012; Heslop et al., 2013, 2014a; Chang et al., 2014].

It is much more common for detrital magnetic particles to occur in the PSD than in the SD size range. Despite the major, and sometimes dominant, contribution of the detrital component (Figure 6c), the moderately interacting SD to PSD signal in core RR0603-03 is weaker than the central ridge signal. This suggests that the detrital component occurs in both noninteracting and interacting stable SD states with a small part of the particle size distribution extending to PSD sizes. The indication of a SD component with wide dispersion (Figure 6a), which tends to be a characteristic of detrital particle assemblages [e.g., Egli, 2004], is surprising given the paucity of reports of nonbiogenic SD particles in sediments. STEM observations provide direct evidence that this component represents SD to PSD inclusions within detrital silicate hosts (Figures 7e–7l). Energy dispersive X-ray spectra (EDS; right) indicate that the inclusions and hosts are crystalline; the inclusions consist of titanomagnetite (Figure 7e, spots 1 and 2) and the host is a silicate (Figure 7e, spot 3). Titanomagnetite inclusions have variable morphologies, including roughly equi-dimensional particles (Figures

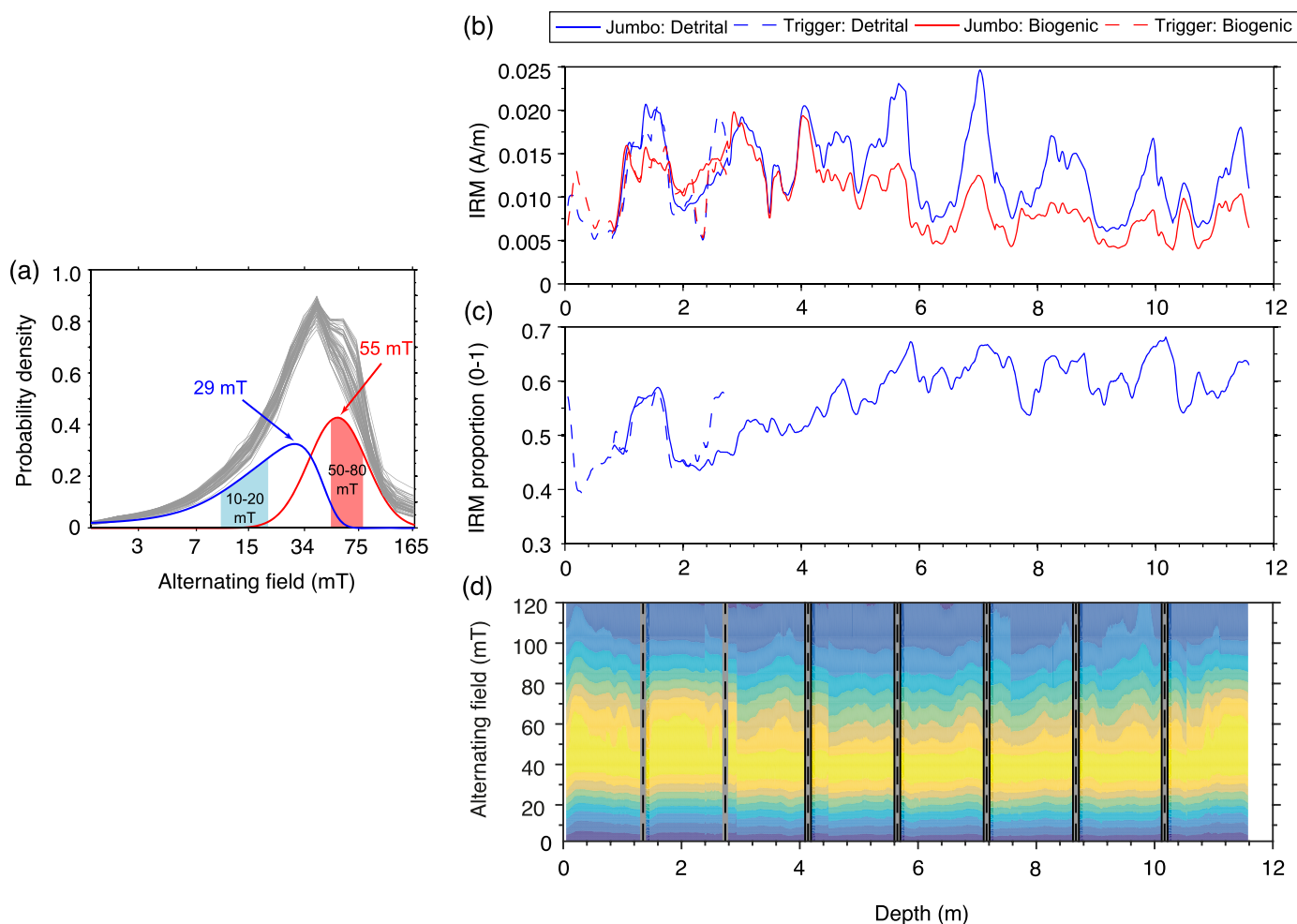


Figure 6. IRM unmixing results for core RR0603-03. (a) Curves (gray) for every 20 cm down-core and skewed generalized Gaussian distributions for the mean of two magnetic components (blue and red) from end-member unmixing of AF demagnetization spectra of an IRM for all 1293 measurements at 1 cm intervals (logarithmic field axis). The sum of the two components gives the average of the gray measured curves. The peak coercivity for each component is indicated. The low-coercivity distribution is skewed to low values and has high dispersion, which is typical of detrital magnetic mineral assemblages. The high-coercivity component has narrow dispersion, which is typical of biogenic magnetite [Egli, 2004]. (b) Down-core variations for the two end-members with respect to magnetization (labeled "detrital" for the low-coercivity and "biogenic" for the high-coercivity components). (c) Proportion of the total IRM contributed by the detrital component. (d) IRM spectra at 1 cm intervals except within ± 10 cm of core breaks (vertical dashed lines with gray shading). Core breaks are represented by gray (black) for the TC (JC). Uniform magnetic properties are indicated by a peak coercivity of ~ 40 mT (yellow) and IRM spectra. Color-scale changes indicate the height with respect to the maximum (yellow) of the normalized spectra.

7e and 7f), elongated particles (Figure 7g), and dendritic textures (Figure 7h). Elemental maps of a particle (Figure 7i) indicate that the host is dominated by Si (Figure 7j) and that inclusions are relatively Fe-rich (Figure 7k) and Ti-poor (Figure 7l). Inclusions with clear igneous textures, including dendrites (Figure 7h), and the abundance of Ti in inclusions provide strong evidence that the particles have an igneous, and not a biogenic, origin. The nanoparticles appear to have no preferred crystallographic orientation and largely occur in the 30–100 nm (i.e., ideal stable SD) size range [e.g., Muxworthy and Williams, 2009], with some inclusions having slightly larger sizes (Figures 7g and 7h). Magnetic particle concentrations within host silicates are high (Figures 7e–7i), which makes them detectable in our bulk magnetic measurements. The images in Figure 7 confirm our interpretation that two SD components dominate the magnetic properties of the studied sediments. The possibility of stable SD magnetite inclusions within larger silicate particles has been widely recognized in the paleomagnetic and environmental magnetic literature, but remained undemonstrated until Chang *et al.* [2016b] provided evidence that they occur widely and are potentially paleomagnetically important.

TEM observations also explain the low-temperature magnetic results, particularly the lack of a Verwey transition that would be expected if magnetite is present. Oxidation, which occurs commonly on the surface of

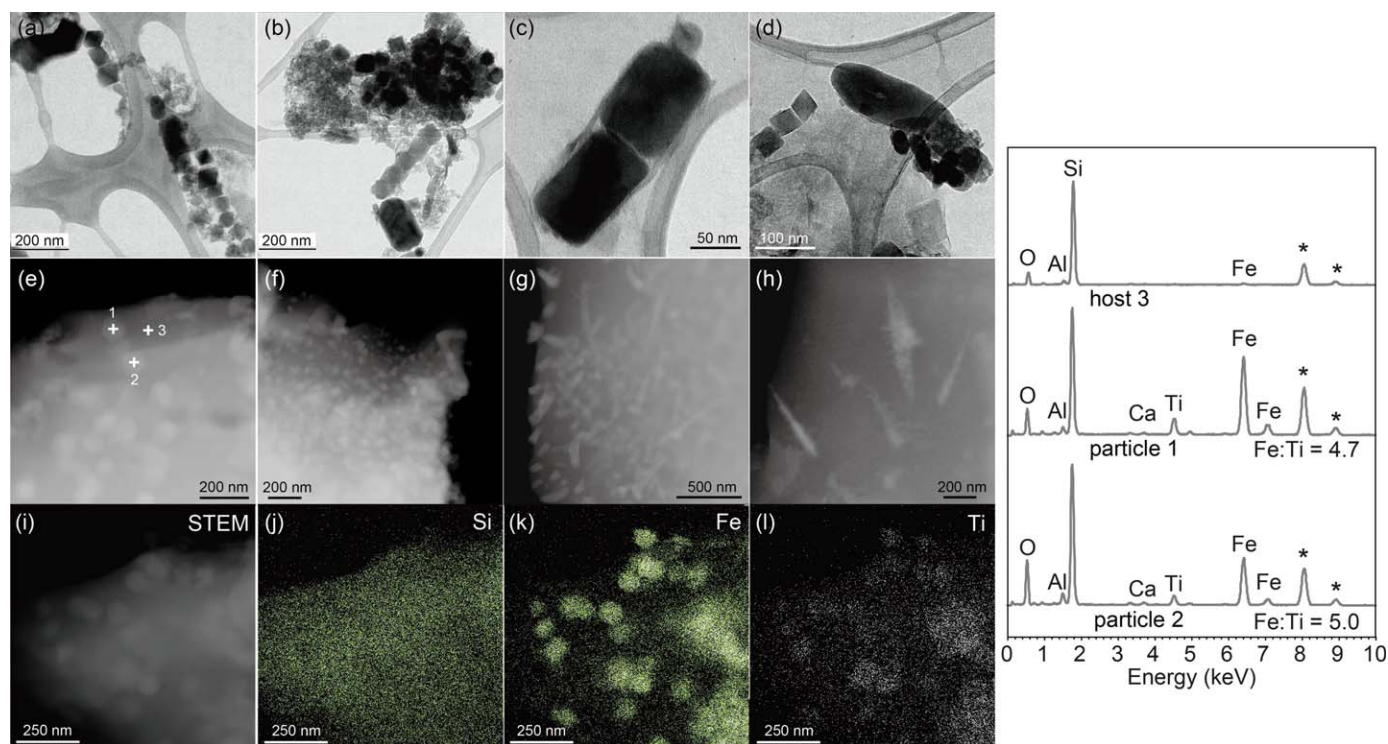


Figure 7. (a–d) Bright-field TEM and (e–l) STEM images of particles in a magnetic extract from core RR0603-03 (core section 2, 60–62 cm depth). (a) Octahedral biogenic magnetite particles (30–100 nm), some of which occur in slightly disrupted chains. (b) Disrupted and intact (with five magnetosome crystals) biogenic magnetite chains. (c) Two cubo-octahedral biogenic magnetite particles (~100 nm long dimension). (d) Disrupted and intact (with three magnetosome crystals) biogenic magnetite chains. (e–i) STEM images of silicate host minerals with titanomagnetite inclusions. EDS spectra (right) indicate that the inclusions are titanomagnetite (spots 1 and 2 in Figure 7e) and that the host is crystalline, with Si and O peaks (i.e., a silicate) (spot 3). Analyses at spots 1 and 2 also contain Si and O peaks because inclusions lie within the silicate and the electron beam interacted with host and inclusion. Titanomagnetite inclusions have variable morphologies, including (e, f) approximately equidimensional particles, (g) elongated particles, and (h) dendritic textures. Titanomagnetite spectra have Fe/Ti ratios of ~5. Elemental maps indicate that (i) a host particle is dominated by (j) Si, and that inclusions are (k) Fe-rich and (l) relatively Ti-poor. The nanoparticles appear to have no preferred crystallographic orientation and largely occur in the ideal stable SD size range (30–100 nm). These images confirm that two SD components dominate the sediment magnetic properties.

biogenic magnetite particles, particularly in pelagic sediments, causes suppression and eventual loss of the Verwey transition signal [Moskowitz *et al.*, 1993; Özdemir *et al.*, 1993; Smirnov and Tarduno, 2000; Chang *et al.*, 2013]. Likewise, Ti substitution within magnetite causes suppression and eventual loss of the Verwey transition signal [Moskowitz *et al.*, 1998]. Thus, low-temperature magnetic properties are consistent with the presence of surficially oxidized biogenic magnetite and titanomagnetite.

Chang *et al.* [2016b] queried whether detrital silicate particles with magnetic nano-inclusions can contribute to sedimentary paleomagnetic signals. Peak coercivities for the two magnetic components in core RR0603-03 are 29 and 55 mT, respectively (Figure 6a). The low-coercivity component (detrital SD titanomagnetite) is dominant at 10–20 mT, with almost no contribution from the high-coercivity component, while the high-coercivity component (biogenic SD magnetite) is dominant at 50–80 mT. Thus, we used slopes of NRM/ARM and NRM/IRM to estimate RPI using NRM, ARM, and IRM demagnetization windows of 10–20 and 50–80 mT, respectively, to assess how the two components contribute to the RPI signal (Figures 8a and 8b), and following Ouyang *et al.* [2014], to assess relative remanence acquisition efficiencies in biogenic and detrital magnetite. Coherence of the recorded RPI signal with the global SINT-2000 stack of Valet *et al.* [2005] demonstrates that the sediments record reliable geomagnetic RPI signals (Figure 4). These results are discussed below.

5. Discussion

For isolated magnetic particles settling in a fluid, the geomagnetic field will exert an aligning torque so that the particles will align fully and almost instantaneously with the field [Nagata, 1961; Tauxe *et al.*, 2006; Roberts *et al.*, 2013a]. This would give rise to perfectly efficient sedimentary magnetizations with 100% particle

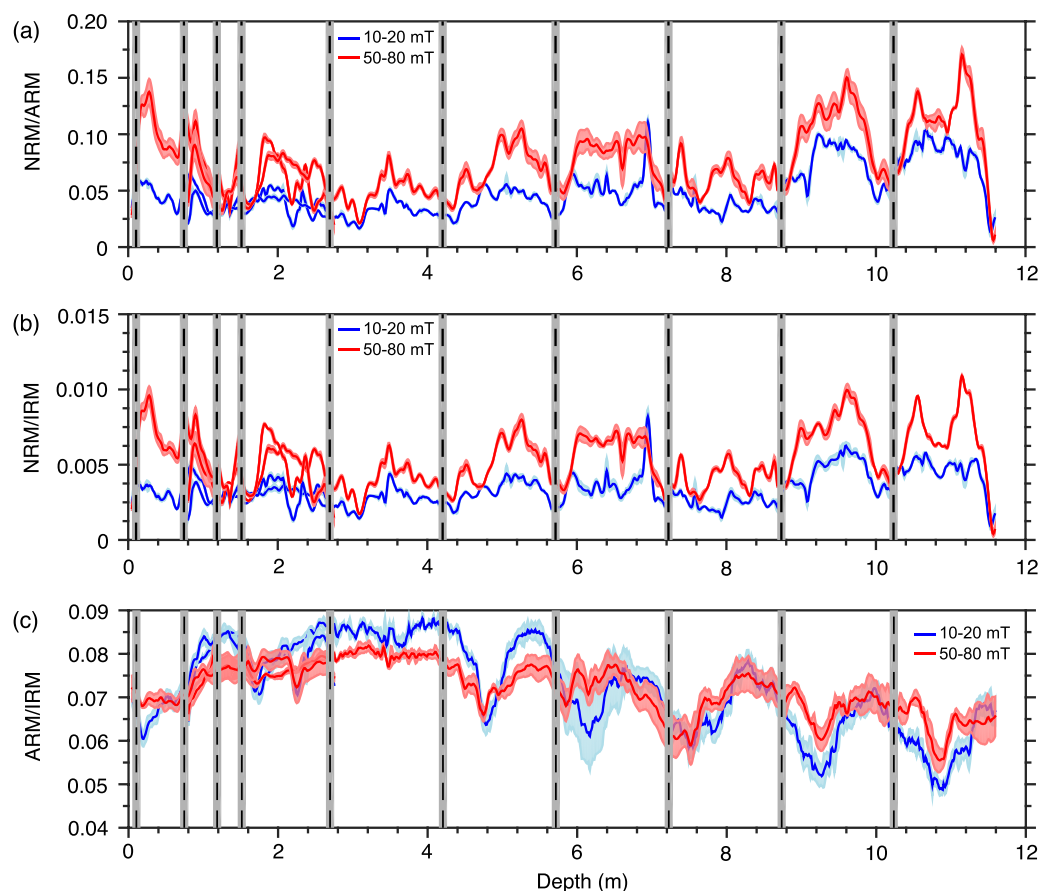


Figure 8. Estimated contribution of two stable SD components to the RPI signal in core RR0603-03. Their respective contributions were estimated by fitting slopes to NRM demagnetization versus ARM demagnetization plots [cf. Channell *et al.*, 2002; Ouyang *et al.*, 2014] over the 10–20 and 50–80 mT ranges for the detrital and biogenic components, respectively, because there is little overlap over these ranges (Figure 6a). (a) NRM/ARM and (b) NRM/IRM normalizations for the detrital (blue with ± 1 standard error shading) and biogenic (red with ± 1 standard error shading) components. (c) ARM/IRM (magnetic particle size proxy) for the two components. Core breaks are indicated by vertical dashed black lines; gray shading indicates the 10 cm at the ends of each section that was removed to avoid magnetometer edge effects.

alignment. Sedimentary paleomagnetic records are much less efficient, typically of the order of a few percent at most [Tauxe *et al.*, 2006; Roberts *et al.*, 2013a; Heslop *et al.*, 2014b]. Our results provide an opportunity to assess paleomagnetic signal acquisition efficiency for both detrital and biogenic magnetic minerals.

5.1. Can Nanoparticle Inclusions Record RPI Variations?

RPI determination over the 10–20 mT demagnetization window yields a similar signal to that over the 50–80 mT window for both ARM and IRM normalizations, but with significantly different amplitudes (Figures 8a and 8b). Furthermore, these normalizations are coherent with the SINT-2000 record of Valet *et al.* [2005]. This indicates that a robust global RPI signal is recorded by core RR0603-03 (Figure 4). It is, therefore, reasonable to ask whether nanoparticle inclusions can record RPI variations. Chang *et al.* [2016b] concluded that particle alignment is possible if crystallographically aligned SD magnetic nanoparticles provide a sufficiently strong net magnetic moment that the geomagnetic field can overcome hydrodynamic torques on particles. Their calculations indicate that such particle alignment is only expected for a limited particle size range and net magnetic moment.

NRM/ARM and NRM/IRM for both the biogenic and detrital components (Figures 8a and 8b) are coherent with the global SINT-2000 signal (Figure 4) [Valet *et al.*, 2005]. The fact that global RPI variations are recorded over the 10–20 mT interval indicates that the detrital SD titanomagnetite inclusions reliably record a paleomagnetic signal. Thus, the concentration of magnetic inclusions must have been sufficient to confer a strong enough net magnetic moment to enough silicate particles that the geomagnetic aligning force

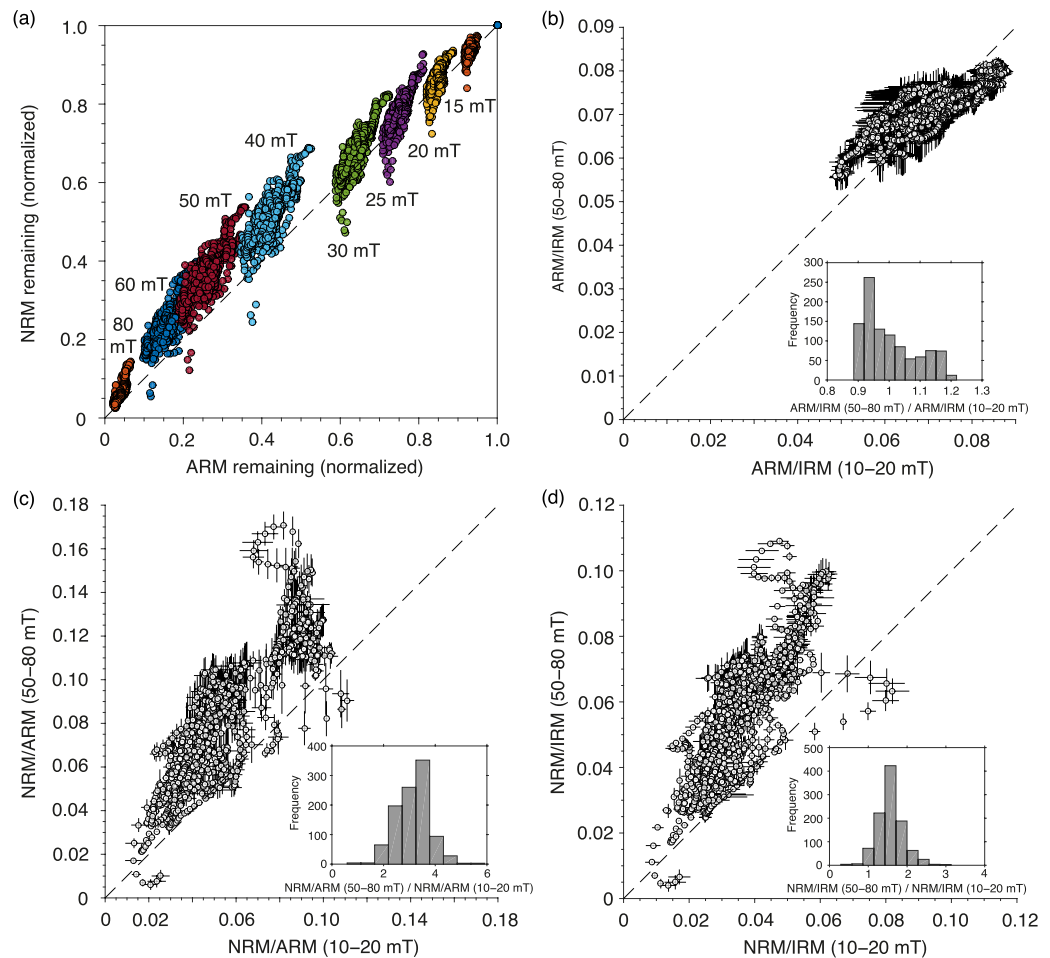


Figure 9. Comparison of remanence acquisition efficiency for biogenic and detrital particles from core RR0603-03. (a) NRM remaining versus ARM remaining at each AF demagnetization step (dashed line gives the 1:1 relationship). The data fall on a curved trend because of the presence of two magnetic components. (b) ARM/IRM for the high-coercivity fraction plotted versus that for the low-coercivity fraction. The data vary around the 1:1 line, which indicates that magnetic particle size is similar for both fractions. (c) NRM/ARM and (d) NRM/IRM for the high-coercivity (biogenic) versus low-coercivity (detrital) components. Most data fall above the 1:1 line, which suggests that the biogenic component has a more efficient magnetization than the detrital component. In histograms of average slopes (insets), biogenic magnetizations are ~2–4 times as efficient as detrital magnetizations for NRM/ARM, but 1–2 times as efficient for NRM/IRM. See text for discussion. Error bars represent ± 1 standard error [York, 1966].

overcame other randomizing forces, including hydrodynamic torques [Heslop, 2007; Chang et al., 2016b]. While our TEM observations could be biased toward identification of magnetofossils and particles with magnetic nanoinclusions, no other magnetic particle types were observed. We argue that the concentration of nanoinclusions is so high (e.g., Figures 7e–7g) that they must be detected in our magnetic measurements. We, therefore, conclude that nanoparticle inclusions enable host silicate particles to record RPI variations. To our knowledge, this is the first verification of this possibility.

5.2. Do the Detrital and Biogenic Components Record RPI Variations With Different Efficiency?

As indicated in Figure 8, both normalizations record similar RPI variations. However, higher NRM/ARM and NRM/IRM slopes are indicated for the biogenic component compared to the detrital component (Figures 8a, 8b, and 9a). This suggests that the magnetic moments of the biogenic component aligned more efficiently with the ambient magnetic field (as long as there is no inherent alignment bias for one type of magnetic particle compared to the other or if there are no significant particle size differences between the two particle types). Concerning the latter possibility, Maher [1988] documented ARM variations over several orders of magnitude across the SD size range, whereas SIRM varies much less. If the two components have different SD particle sizes, they could have different intrinsic paleomagnetic recording efficiency. This possibility can be tested roughly by comparing the respective down-core ARM/IRM variations (Figure 8c). The

two components are variable, and sometimes have the same values, while in other intervals one component has finer particle sizes than the other. Overall, ARM/IRM data for the two components fall on a 1:1 line (Figure 9b), so we conclude that particle size differences cannot have given rise to a systematic recording bias where the detrital SD component has an almost universally weaker RPI contribution with respect to the SD magnetofossil component. We cannot assess easily how variable magnetic inclusion orientations in host particles (Figures 7e–7h) contribute to paleomagnetic recording compared to intact magnetofossil chains. Nevertheless, higher NRM/ARM and NRM/IRM values indicate a far superior recording capability for magnetofossils compared to magnetic nano-inclusions. Despite this, Mao *et al.* [2014] argued that alignment efficiency can be as low as $\leq 1\%$ for sedimentary magnetofossil magnetizations.

We now compare our results with those of Ouyang *et al.* [2014] who demonstrated that biogenic magnetite is ~ 2 – 4 times more efficiently magnetized than detrital PSD magnetite (for both NRM/ARM and NRM/IRM). For core RR0603-03, the SD biogenic component is also 2–4 times more efficiently magnetized than the SD detrital component for NRM/ARM (Figure 9c, histogram). However, the biogenic component is only 1–2 times more efficiently magnetized than the detrital component for NRM/IRM (Figure 9d, histogram). This probably results from the fact that for SD (titano-)magnetite, IRM does not vary much [Day *et al.*, 1977; Maher, 1988] so that NRM/IRM will be similar for two SD components. However, IRM is much different for SD compared to PSD particles, so that NRM/IRM will contrast more than for two SD components. Regardless, NRM/IRM is almost always larger for the biogenic compared to the detrital SD component in core RR0603-03. Thus, all analyses indicate that SD biogenic magnetite carries a more efficient NRM record than detrital SD titanomagnetite inclusions in the studied sediments.

5.3. What Are the Implications of Differential Acquisition Efficiencies for RPI Signal Recording?

RPI for both components in core RR0603-03 generally has in-phase variations (Figures 8a and 8b). This is because each component is controlled climatically (compare Figures 2 and 6b). In this case, RPI recording is straightforward. Different remanence acquisition efficiencies for the biogenic and detrital components do not appear to have important consequences because both record the same signal and give rise to coherent overall recording. Such a situation is apparently common in some depositional environments, such as pelagic carbonates, where detrital and biogenic magnetizations often vary in phase with each other [Roberts *et al.*, 2011; Yamazaki, 2012; Yamazaki and Ikehara, 2012]. However, the low deposition rate of such sediments means that pelagic carbonates are not ideal for obtaining high-resolution geomagnetic records. In many sediments, detrital and biogenic magnetizations do not always vary in phase with each other [e.g., Just *et al.*, 2012; Heslop *et al.*, 2013], so that the overall impact of differential recording efficiency will be non-trivial. This suggests that component-by-component understanding of paleomagnetic recording efficiency needs to become a routine aspect of sedimentary RPI analysis.

Acknowledgments

The authors acknowledge funding support from: L.C.: China Scholarship Council; A.P.R. and D.H.: Australian Research Council (ARC) through grants DP120103952, DP140104544, and LE120100218; H.V.M.: ARC Future Fellowship FT140100286; E.J.R.: ARC Australian Laureate Fellowship FL120100050; and H.P.: European Research Council grant 617462. We thank Joe Stoner, Marine Geology Repository (MGR), Oregon State University (OSU), for facilitating sampling of the studied sediment core (MGR is supported by NSF grant OCE-1558679), Maziet Cheseby (MGR, OSU) for technical support, and Suzanne MacLachlan and Guy Rothwell, BOSCORF, National Oceanography Centre Southampton, for performing the XRF analyses. Data presented in this paper will be uploaded into the MagIC database (<https://www2.earthref.org/MagIC>).

6. Conclusions

Reliable geomagnetic relative paleointensity signals in the studied eastern equatorial Pacific Ocean sediment core are carried by two stable SD magnetic components (magnetite magnetofossils and titanomagnetite inclusions within larger silicate host particles). We document for the first time that magnetic nano-inclusions within host silicate particles are capable of recording a reliable sedimentary magnetization. This magnetization is much less efficient than that carried by cooccurring magnetite magnetofossils. The lower recording efficiency of inclusions probably results from variable net magnetic moment and variable host particle size in relation to the key balance between aligning geomagnetic torques and randomizing hydrodynamic torques that act on magnetic particles [Heslop, 2007; Chang *et al.*, 2016b]. In relative paleointensity analysis, sediments are generally treated as homogeneous with no variability in relative recording efficiency of different magnetic mineral components. Our work demonstrates that this is not a safe assumption and that a more detailed assessment of paleomagnetic recording by different magnetic components needs to become a routine part of sedimentary relative paleointensity analysis.

References

- Barber, R., and F. Chavez (1991), Regulation of primary productivity rate in the equatorial Pacific, *Limnol. Oceanogr.*, *36*, 1803–1815.
Chang, L., A. P. Roberts, W. Williams, J. D. Fitz Gerald, J. C. Larrasoana, L. Jovane, and A. R. Muxworthy (2012), Giant magnetofossils and hyperthermal events, *Earth Planet. Sci. Lett.*, *351*–*352*, 258–269.

- Chang, L., M. Winklhofer, A. P. Roberts, D. Heslop, F. Florindo, M. J. Dekkers, W. Krijgsman, K. Kodama, and Y. Yamamoto (2013), Low-temperature magnetic properties of pelagic carbonates: Oxidation of biogenic magnetite and identification of magnetosome chains, *J. Geophys. Res. Solid Earth*, *118*, 6049–6065, doi:10.1002/2013JB010381.
- Chang, L., A. P. Roberts, M. Winklhofer, D. Heslop, M. J. Dekkers, W. Krijgsman, J. D. Fitz Gerald, and P. Smith (2014), Magnetic detection and characterization of biogenic magnetic minerals: A comparison of ferromagnetic resonance and first-order reversal curve diagrams, *J. Geophys. Res. Solid Earth*, *119*, 6136–6158, doi:10.1002/2014JB011213.
- Chang, L., D. Heslop, A. P. Roberts, D. Rey, and K. J. Mohamed (2016a), Discrimination of biogenic and detrital magnetite through a double Verwey transition temperature, *J. Geophys. Res. Solid Earth*, *121*, 3–14, doi:10.1002/2015JB012485.
- Chang, L., A. P. Roberts, D. Heslop, A. Hayashida, J. H. Li, X. Zhao, W. Tian, and Q. H. Huang (2016b), Widespread occurrence of silicate-hosted magnetic mineral inclusions in marine sediments and their contribution to paleomagnetic recording, *J. Geophys. Res. Solid Earth*, *121*, 8415–8431, doi:10.1002/2016JB013109.
- Channell, J. E. T., and L. Lanci (2014), Oligocene-Miocene relative (geomagnetic) paleointensity correlated from the equatorial Pacific (IODP Site U1334 and ODP Site 1218) to the South Atlantic (ODP Site 1090), *Earth Planet. Sci. Lett.*, *387*, 77–88.
- Channell, J. E. T., A. Mazaud, P. Sullivan, S. Turner, and M. E. Raymo (2002), Geomagnetic excursions and paleointensities in the 0.9–2.15 Ma interval of the Matuyama Chron at ODP Site 983 and 984 (Iceland Basin), *J. Geophys. Res.*, *107*(B6), 2114, doi:10.1029/2001JB000491.
- Channell, J. E. T., C. Xuan, and D. A. Hodell (2009), Stacking paleointensity and oxygen isotope data for the last 1.5 Myr (PISO-1500), *Earth Planet. Sci. Lett.*, *283*, 14–23.
- Channell, J. E. T., D. A. Hodell, B. S. Singer, and C. Xuan (2010), Reconciling astrochronological and $^{40}\text{Ar}/^{39}\text{Ar}$ ages for the Matuyama-Brunhes boundary and late Matuyama Chron, *Geochem. Geophys. Geosyst.*, *11*, Q0AA12, doi:10.1029/2010GC003203.
- Channell, J. E. T., D. A. Hodell, and J. H. Curtis (2016), Relative paleointensity (RPI) and oxygen isotope stratigraphy at IODP Site U1308: North Atlantic RPI stack for 1.2–2.2 Ma (NARPI-2200) and age of the Olduvai Subchron, *Quat. Sci. Rev.*, *131*, 1–19.
- Day, R., M. Fuller, and V. A. Schmidt (1977), Hysteresis properties of titanomagnetites: Grain-size and compositional dependence, *Phys. Earth Planet. Inter.*, *13*, 260–267.
- Dunlop, D. J. (2002), Theory and application of the Day plot (M_r/M_s versus H_c/H_c): 2. Application to data for rocks, sediments, and soils, *J. Geophys. Res.*, *107*(B3), 2056, doi:10.1029/2001JB000487.
- Dymond, J., E. Suess, and M. Lyle (1992), Barium in deep-sea sediment: A geochemical proxy for paleoproductivity, *Paleoceanography*, *7*, 163–181.
- Edwards, A. M., T. Platt, and S. Sathyendranath (2004), The high-nutrient, low-chlorophyll regime of the ocean: Limits on biomass and nitrate before and after iron enrichment, *Ecol. Model.*, *171*, 103–125.
- Egli, R. (2003), Analysis of the field dependence of remanent magnetization curves, *J. Geophys. Res.*, *108*(B2), 2081, doi:10.1029/2002JB002023.
- Egli, R. (2004), Characterization of individual rock magnetic components by analysis of remanence curves, 1. Unmixing natural sediments, *Stud. Geophys. Geod.*, *48*, 391–446.
- Egli, R., A. P. Chen, M. Winklhofer, K. P. Kodama, and C. S. Horng (2010), Detection of noninteracting single domain particles using first-order reversal curve diagrams, *Geochem. Geophys. Geosyst.*, *11*, Q01Z11, doi:10.1029/2009GC002916.
- Govin, A., U. Holzwarth, D. Heslop, L. Ford Keeling, M. Zabel, S. Multiza, J. A. Collins, and C. M. Chiessi (2012), Distribution of major elements in Atlantic surface sediments (36°N–49°S): Imprint of terrigenous input and continental weathering, *Geochem. Geophys. Geosyst.*, *13*, Q01013, doi:10.1029/2011GC003785.
- Guyodo, Y., and J.-P. Valet (1999), Global changes in intensity of the Earth's magnetic field during the past 800 kyr, *Nature*, *399*, 249–252.
- Hale, S. B. (2008), Paleoproductivity variations in the eastern central equatorial Pacific Ocean on glacial timescales, MS thesis, Univ. Indiana, Bloomington.
- Heslop, D. (2007), Are hydrodynamic shape effects important when modelling the formation of depositional remanent magnetization?, *Geophys. J. Int.*, *171*, 1029–1035.
- Heslop, D., and M. Dillon (2007), Unmixing magnetic remanence curves without *a priori* knowledge, *Geophys. J. Int.*, *170*, 556–566.
- Heslop, D., and A. P. Roberts (2012a), Estimation of significance levels and confidence intervals for first-order reversal curve distributions, *Geochem. Geophys. Geosyst.*, *13*, Q12Z40, doi:10.1029/2012GC004115.
- Heslop, D., and A. P. Roberts (2012b), A method for unmixing magnetic hysteresis loops, *J. Geophys. Res.*, *117*, B03103, doi:10.1029/2011JB008859.
- Heslop, D., A. P. Roberts, L. Chang, M. Davies, A. Abrajevitch, and P. De Deckker (2013), Quantifying magnetite magnetofossil contributions to sedimentary magnetizations, *Earth Planet. Sci. Lett.*, *382*, 58–65.
- Heslop, D., A. P. Roberts, and L. Chang (2014a), Recognition of biogenic magnetite components from first-order reversal curve signatures, *Geochem. Geophys. Geosyst.*, *15*, 2170–2179, doi:10.1002/2014GC005291.
- Heslop, D., A. P. Roberts, and R. Hawkins (2014b), A statistical simulation of magnetic particle alignment in sediments, *Geophys. J. Int.*, *197*, 828–837.
- Horng, C.-S., M.-Y. Lee, H. Pälike, K.-Y. Wei, W.-T. Liang, Y. Iizuka, and M. Torii (2002), Astronomically calibrated ages for geomagnetic reversals within the Matuyama chron, *Earth Planets Space*, *54*, 679–690.
- Just, J., M. J. Dekkers, T. von Dobeneck, A. van Hoesel, and T. Bickert (2012), Signatures and significance of aeolian, fluvial, bacterial and diagenetic magnetic mineral fractions in Late Quaternary marine sediments off Gambia, NW Africa, *Geochem. Geophys. Geosyst.*, *13*, Q0A002, doi:10.1029/2012GC004146.
- King, J. W., S. K. Banerjee, and J. Marvin (1983), A new rock-magnetic approach to selecting sediments for geomagnetic paleointensity studies: Application to paleointensity for the last 4000 years, *J. Geophys. Res.*, *88*, 5911–5921.
- Kirschvink, J. L. (1980), The least-squares line and plane and the analysis of palaeomagnetic data, *Geophys. J. R. Astron. Soc.*, *62*, 699–718.
- Kopp, R. E., and J. L. Kirschvink (2008), The identification and biogeochemical interpretation of fossil magnetotactic bacteria, *Earth Sci. Rev.*, *86*, 42–61.
- Laj, C., and J. E. T. Channell (2015), Geomagnetic excursions, in *Treatise on Geophysics, Geomagnetism*, vol. 5, edited by M. Kono, 2nd ed., pp. 343–382, Elsevier, Oxford, U. K.
- Laj, C., C. Kissel, A. Mazaud, J. E. T. Channell, and J. Beer (2000), North Atlantic palaeointensity stack since 75 ka (NAPIS-75) and the duration of the Laschamp event, *Philos. Trans. R. Soc. London A*, *358*, 1009–1025.
- Larrasoana, J. C., A. P. Roberts, L. Chang, S. A. Schellenberg, J. D. Fitz Gerald, R. D. Norris, and J. C. Zachos (2012), Magnetotactic bacterial response to Antarctic dust supply during the Palaeocene-Eocene thermal maximum, *Earth Planet. Sci. Lett.*, *333–334*, 122–133.
- Levi, S., and S. K. Banerjee (1976), On the possibility of obtaining relative paleointensities from lake sediments, *Earth Planet. Sci. Lett.*, *29*, 219–226.

- Lisiecki, L. E., and M. E. Raymo (2009), Diachronous benthic $\delta^{18}\text{O}$ responses during late Pleistocene terminations, *Paleoceanography*, *24*, PA3210, doi:10.1029/2009PA001732.
- Liu, Q. S., A. P. Roberts, E. J. Rohling, R. X. Zhu, and Y. B. Sun (2008), Post-depositional remanent magnetization lock-in and the location of the Matuyama-Brunhes geomagnetic reversal boundary in marine and Chinese loess sequences, *Earth Planet. Sci. Lett.*, *275*, 102–110.
- Loubere, P. (2000), Marine control of biological production in the eastern equatorial Pacific Ocean, *Nature*, *406*, 497–500.
- Lurcock, P. C., and G. S. Wilson (2012), PuffinPlot: A versatile, user-friendly program for paleomagnetic analysis, *Geochem. Geophys. Geosyst.*, *13*, Q06Z45, doi:10.1029/2012GC004098.
- Lyle, M. W., H. Pälike, T. C. Moore, N. Mitchell, and J. Backman (2006), *Summary Report of R/V Roger Revelle Site Survey AMAT03 to the IODP Environmental Protection and Safety Panel (EPSP) in Support for Proposal IODP626*, 144 pp., Univ. of Southampton, Southampton, U. K.
- Maher, B. A. (1988), Magnetic properties of some synthetic sub-micron magnetites, *Geophys. J.*, *94*, 83–96.
- Mao, X. G., R. Egli, N. Petersen, M. Hanzlik, and X. Y. Zhao (2014), Magnetotaxis and acquisition of detrital remanent magnetization by magnetotactic bacteria in natural sediment: First experimental results and theory, *Geochem. Geophys. Geosyst.*, *15*, 255–283, doi:10.1002/2013GC005034.
- Martínez-Botí, M. A., G. Marino, G. L. Foster, P. Ziveri, M. J. Henehan, P. G. Mortyn, and D. Vance (2015), Boron isotope evidence for oceanic carbon dioxide leakage during the last deglaciation, *Nature*, *518*, 219–222.
- Mitchell, N. C., M. W. Lyle, M. B. Knappenberger, and L. M. Liberty (2003), Lower Miocene to present stratigraphy of the equatorial Pacific sediment bulge and carbonate dissolution anomalies, *Paleoceanography*, *18*(2), 1038, doi:10.1029/2002PA000828.
- Moskowitz, B. M., R. B. Frankel, and D. A. Bazylinski (1993), Rock magnetic criteria for the detection of biogenic magnetite, *Earth Planet. Sci. Lett.*, *120*, 283–300.
- Moskowitz, B. M., M. Jackson, and C. Kissel (1998), Low temperature magnetic behavior of titanomagnetites, *Earth Planet. Sci. Lett.*, *157*, 141–149.
- Muxworthy, A. R., and D. J. Dunlop (2002), First-order reversal curve (FORC) diagrams for pseudo-single-domain magnetites at high temperature, *Earth Planet. Sci. Lett.*, *203*, 369–382.
- Muxworthy, A. R., and W. Williams (2009), Critical superparamagnetic/single domain grain sizes in interacting magnetite particles: Implications for magnetosome crystals, *J. R. Soc. Interface*, *6*, 1207–1212.
- Nagata, T. (1961), *Rock Magnetism*, 350 pp., Maruzen, Tokyo.
- Ouyang, T., D. Heslop, A. P. Roberts, C. Tian, Z. Zhu, Y. Qiu, and X. Peng (2014), Variable remanence acquisition efficiency in sediments containing biogenic and detrital magnetites: Implications for relative paleointensity signal recording, *Geochem. Geophys. Geosyst.*, *15*, 2780–2796, doi:10.1002/2014GC005301.
- Özdemir, Ö., D. J. Dunlop, and B. M. Moskowitz (1993), The effect of oxidation on the Verwey transition in magnetite, *Geophys. Res. Lett.*, *20*, 1671–1674.
- Paterson, G. A., Y. Wang, and Y. Pan (2013), The fidelity of paleomagnetic records carried by magnetosome chains, *Earth Planet. Sci. Lett.*, *383*, 82–91.
- Pike, C. R., A. P. Roberts, and K. L. Verosub (1999), Characterizing interactions in fine magnetic particle systems using first order reversal curves, *J. Appl. Phys.*, *85*, 6660–6667.
- Rea, D. K., N. G. Pisias, and T. Newberry (1991), Late Pleistocene paleoclimatology of the central equatorial Pacific: Flux patterns of biogenic sediments, *Paleoceanography*, *6*, 227–244.
- Roberts, A. P. (2008), Geomagnetic excursions: Knowns and unknowns, *Geophys. Res. Lett.*, *35*, L17307, doi:10.1029/2008GL034719.
- Roberts, A. P., C. R. Pike, and K. L. Verosub (2000), First-order reversal curve diagrams: A new tool for characterizing the magnetic properties of natural samples, *J. Geophys. Res.*, *105*, 28,461–28,475.
- Roberts, A. P., F. Florindo, G. Villa, L. Chang, L. Jovane, S. M. Bohaty, J. C. Larrasoña, D. Heslop, and J. D. Fitz Gerald (2011), Magnetotactic bacterial abundance in pelagic marine environments is limited by organic carbon flux and availability of dissolved iron, *Earth Planet. Sci. Lett.*, *310*, 441–452.
- Roberts, A. P., L. Chang, D. Heslop, F. Florindo, and J. C. Larrasoña (2012), Searching for single domain magnetite in the “pseudo-single-domain” sedimentary haystack: Implications of biogenic magnetite preservation for sediment magnetism and relative paleointensity determinations, *J. Geophys. Res.*, *117*, B08104, doi:10.1029/2012JB009412.
- Roberts, A. P., L. Tauxe, and D. Heslop (2013a), Magnetic paleointensity stratigraphy and high-resolution Quaternary geochronology: Successes and future challenges, *Quat. Sci. Rev.*, *61*, 1–16.
- Roberts, A. P., F. Florindo, L. Chang, D. Heslop, L. Jovane, and J. C. Larrasoña (2013b), Magnetic properties of pelagic marine carbonates, *Earth Sci. Rev.*, *127*, 111–139.
- Skinner, L. C., and N. J. Shackleton (2005), An Atlantic lead over Pacific deep-water change across Termination I: Implications for the application of the marine isotope stage stratigraphy, *Quat. Sci. Rev.*, *24*, 571–580.
- Smirnov, A. V., and J. A. Tarduno (2000), Low-temperature magnetic properties of pelagic sediments (Ocean Drilling Program Site 805C): Tracers of maghemitization and magnetic mineral reduction, *J. Geophys. Res.*, *105*, 16,457–16,471.
- Stoner, J. S., C. Laj, J. E. T. Channell, and C. Kissel (2002), South Atlantic and North Atlantic geomagnetic paleointensity stacks (0–80 ka): Implications for inter-hemispheric correlation, *Quat. Sci. Rev.*, *21*, 1141–1151.
- Suganuma, Y., M. Okada, K. Horie, H. Kaiden, M. Takehara, R. Senda, J.-I. Kimura, K. Kawamura, Y. Haneda, O. Kazaoka, and M. J. Head (2015), Age of Matuyama-Brunhes boundary constrained by U-Pb zircon dating of a widespread tephra, *Geology*, *43*, 491–494.
- Takahashi, T., et al. (2004), Climatological mean and decadal change in surface ocean $p\text{CO}_2$, and net sea–air CO_2 flux over the global oceans, *Deep Sea Res., Part II*, *56*, 554–577.
- Tauxe, L. (1993), Sedimentary records of relative paleointensity of the geomagnetic field: Theory and practice, *Rev. Geophys.*, *31*, 319–354.
- Tauxe, L., T. Herbert, N. J. Shackleton, and Y. S. Kok (1996), Astronomical calibration of the Matuyama-Brunhes boundary: Consequences for magnetic remanence acquisition in marine carbonates and the Asian loess sequences, *Earth Planet. Sci. Lett.*, *140*, 133–146.
- Tauxe, L., J. L. Steindorf, and A. Harris (2006), Depositional remanent magnetization: Toward an improved theoretical and experimental foundation, *Earth Planet. Sci. Lett.*, *244*, 515–529.
- Valet, J. P., L. Meynadier, and Y. Guyodo (2005), Geomagnetic dipole strength and reversal rate over the past two million years, *Nature*, *435*, 802–805.
- Verwey, E. J. W. (1939), Electronic conduction of magnetite (Fe_3O_4) and its transition point at low temperatures, *Nature*, *144*, 327–328.
- Weeks, R., C. Laj, L. Endignoux, M. Fuller, A. Roberts, R. Manganne, E. Blanchard, and W. Goree (1993), Improvements in long core measurement techniques: Applications in palaeomagnetism and palaeoceanography, *Geophys. J. Int.*, *114*, 651–662.
- Winckler, G., R. F. Anderson, S. L. Jaccard, and F. Marcantonio (2016), Ocean dynamics, not dust, have controlled equatorial Pacific productivity over the past 500,000 years, *Proc. Natl. Acad. Sci. U. S. A.*, *113*, 6119–6124.

- Wyrтки, K. (1966), Oceanography of the eastern equatorial Pacific Ocean, *Oceanogr. Mar. Biol. Ann. Rev.*, *4*, 33–68.
- Yamazaki, T. (2012), Paleoposition of the intertropical convergence zone in the eastern Pacific inferred from glacial-interglacial changes in terrigenous and biogenic magnetic mineral fractions, *Geology*, *40*, 151–154.
- Yamazaki, T., and M. Ikehara (2012), Origin of magnetic mineral concentration variation in the Southern Ocean, *Paleoceanography*, *27*, PS2206, doi:10.1029/2011PA002271.
- Yamazaki, T., and H. Oda (2005), A geomagnetic paleointensity stack between 0.8 and 3.0 Ma from equatorial Pacific sediment cores, *Geochem. Geophys. Geosyst.*, *6*, Q11H20, doi:10.1029/2005GC001001.
- York, D. (1966), Least-squares fitting of a straight line, *Can. J. Phys.*, *44*, 1079–1086.
- Zhao, X., D. Heslop, and A. P. Roberts (2015), A protocol for variable-resolution first-order reversal curve measurements, *Geochem. Geophys. Geosyst.*, *16*, 1364–1377, doi:10.1002/2014GC005680.
- Ziegler, L. B., C. G. Constable, C. L. Johnson, and L. Tauxe (2011), PADM2M: A penalized maximum likelihood model of the 0–2 Ma palaeomagnetic axial dipole moment, *Geophys. J. Int.*, *184*, 1069–1089.